CCFE
CULHAM CENTRE FOR FUSION ENERGY

UK Atomic Energy Authority

UKAEA-CCFE-PR(25)264

S. Ahmed, J. T. Omotani, S. L. Newton, J. Birch, F. Militello

STORM modelling of scrape-off layer filament behaviour with hot ions

STORM modelling of scrape-off layer filament behaviour with hot ions

S. Ahmed, J. T. Omotani, S. L. Newton, J. Birch, F. Militello

This is a preprint of a paper submitted for publication in
Plasma Physics and Controlled Fusion

STORM modelling of scrape-off layer filament behaviour with hot ions

S. Ahmed[1,2], J. T. Omotani[1], S. L. Newton[1], J. Birch[1,3] and F. Militello[1]

[1] United Kingdom Atomic Energy Authority, Culham Science Centre, Abingdon, Oxon, OX14 3DB, UK

[2] Department of Physics, University of Bath, Claverton Down, Bath, BA2 7AY, UK

[3] Physics and Astronomy, University of Exeter, North Park Road, Exeter, EX4 4QL, UK

E-mail: john.omotani@ukaea.uk

Abstract. Advances in edge and scrape-off layer diagnostics have shown that often the ion temperature is higher than the electron temperature in scrape-off layer filaments. We have therefore extended the STORM model beyond the cold ion limit commonly used, to include hot ion effects. We find that filaments are both faster and more coherent than in a cold ion model, resulting in increased particle transport. We trace the differences back to the effect of individual hot ion terms, compared using an isothermal ion model. Evolving ion temperature has a modest additional effect on net particle transport, but an ion temperature perturbation in a filament can counteract the instability caused by an electron temperature perturbation.

Keywords: tokamak, scrape-off layer, filaments, plasma exhaust

1. Introduction

The first wall of a magnetic confinement fusion device directly faces the plasma, and all power and particle loads to this wall are of concern if we are to maintain a reliable fusion operation regime [1]. The understanding of the behaviour in the space between the plasma edge and wall has transformed from a diffusion dominated picture, to one in which individual filaments of plasma propagate to the wall, and possibly a combination of the two [2, 3, 4]. In the plasma core, magnetic field lines map out closed magnetic flux surfaces, which allow good plasma confinement. However at the plasma edge, there is a transition at the separatrix to open magnetic field lines, which intersect the first wall in dedicated power handling regions, such as the divertor target plates in X-point magnetic geometries. Fast flow of electrons along field lines, combined with the effect of finite particle orbit size, change in geometry and neutral particle population, makes the formulation of comprehensive edge models difficult, and a current research focus of the field.

Much progress has been made in the study of simplified models, reproducing the existence of the edge filaments and understanding many of the influences on their behaviour, such as filament size or target temperature profile. Many of these studies are discussed in the comprehensive review by D'Ippolito *et al.* [8] and were typically done assuming the ions were cold, which allows the simplification of neglecting finite ion Larmor radius effects. There has been a lot of recent interest in improving on this, due to accumulating experimental evidence that the ion temperature can be higher than the electron temperature at the midplane, whilst these temperatures have a tendency to equilibrate at higher density nearer the target [9, 10, 11].

The basic description of cold ion filaments has essentially a two regime split, into large diameter filaments which strongly interact with the sheath potential (sheath-limited) of the plasma in front of the target plates [2], and small diameter filaments, in which the gradients arising due to large perturbation amplitudes can lead to dominant polarisation effects (inertial regime) [13]. Analytic expressions for the filament radial speed show an increase with diameter in the inertial regime, which falls off on entering the sheath-limited regime. Commonly observed filament diameters on the MAST tokamak [49, 50, 51], for example, are found to be around the transition region [46, 8].

The effect of the electron temperature profile across the filament - introduced by the temperature profile at the sheath boundary or the adiabatic parallel electron response in filaments disconnected from the sheath - is to make the filament spin around its axis and typically slow its radial motion [14, 31]. Various mechanisms of disconnection are thought possible, including high neutral density in detached plasmas or finite length filaments produced by crossing the separatrix in X-point geometry [15]. These effects can also be associated with poloidal variation of the drive for the filament radial motion [16, 17], so the resulting effect on filament motion is difficult to predict.

The introduction of finite ion temperature evolution affects the strength of the radial drive, the filament spin, and affects the coherence of moving filaments through viscosity [18, 19, 20]. 2D models formed by assuming closures representing parallel dynamics, through to turbulence simulation codes such as GBS, have been used to simulate approximations to the hot ion fluid equations in a pure plasma and study the effect on filament motion [19, 21, 22, 23, 24, 20]. Increased small filament coherence has been observed, and the two-regime analytic speed scaling with filament diameter extended to a three-regime form [24, 20], differentiating filament diameter effects in the inertial regime. However, these studies are in their early phases, and understanding the simulated filament speed in light of the predictions is ongoing. Furthermore, the combination of hot ion effects with electromagnetic modifications [25, 32] and neutral physics [26, 19, 27, 28] is on the horizon.

Here we present the results of the first filament study allowing for finite ion temperature influences with the STORM edge simulation model. A module in the BOUT++ framework [29, 30], STORM has been used extensively to study edge filament dynamics [31, 32]. We contrast the filament behaviour in the presence of the hot ion effects, aiming to understand the physical influence of the terms as they are added to

the model and acting as a benchmark for future enhancements of STORM. In section 2 we briefly outline the STORM model and introduce the additional hot ion terms which will be considered. Section 3 describes the numerical methods and initialisation of the simulations and presents a cold ion reference case. In section 4, we present the simulation results as the hot ion terms are introduced one by one, focusing on the impact of the hot ion effects on filament coherence and propagation distance - that is the elements which will allow strong interaction with a tokamak first wall. We summarise this study with a discussion in section 5. Animated versions of figures 1, 4, 6, 7, and 11 are included as supplementary material with the online version of this article.

2. STORM model

Models suitable for describing the cooler edge plasma, where large amplitude fluctuations relative to the background can be expected, are often formulated by applying a collisional closure to the basic density, parallel velocity and energy moment equations [7]. This was done to produce the cold ion, electrostatic version of the STORM model [48, 57], which is a module developed within the BOUT++ simulation framework [29, 30]. Focusing on pure plasmas consisting of one ion species and electrons, the Braginskii [12] description of the inter-species parallel collisional friction and electron heat flux was used, and the electron stress tensor neglected as small in the electron mass, whilst electron inertia was retained. The binormal heat flux given by Braginskii [12] was included but the cross-field collisional transport is expected to be dominated by the turbulent effects present in the system, so a simple cross-field diffusion was introduced (to all but the parallel momentum equations) to provide a lower limit to the cross-field transport and numerical stability. The ion continuity equation is replaced by the vorticity equation, in which cancellations inherent in quasineutrality are accounted for [48, 5, 6]. This can avoid the need to determine the cross-field flows to high order, especially the ion polarisation flow, which may be treated recursively when only small amplitude fluctuations are of interest. The STORM model was recently extended to treat electromagnetic effects in the plasma edge [32]. For the parameters used here, the effect of the magnetic perturbations on the results is negligible, but the terms are included in the simulations as they allow a longer step to be taken by the time-solver [33], as discussed in section 2.2.

2.1. Cold ion STORM equations

The set of equations solved in the electromagnetic cold ion STORM model are the following:

$$\begin{aligned}\frac{\partial n}{\partial t} = & -V_{e\parallel}\nabla_\parallel n - \frac{1}{B}\mathbf{b}\times\nabla\phi\cdot\nabla n - nB\nabla_\parallel\left(\frac{V_{e\parallel}}{B}\right) \\ & + \frac{1}{e}\nabla\times\left(\frac{\mathbf{b}}{B}\right)\cdot\nabla p_e - n\nabla\times\left(\frac{\mathbf{b}}{B}\right)\cdot\nabla\phi + S_n + \nabla\cdot\left(D_\perp\nabla_\perp n\right),\end{aligned}$$

(electron continuity) (1)

$$\frac{\partial}{\partial t}\left(V_{i\parallel}+\frac{e}{m_i}A_\parallel\right) = -V_{i\parallel}\nabla_\parallel V_{i\parallel} - \frac{1}{B}\mathbf{b}\times\nabla\phi\cdot\nabla V_{i\parallel} - \frac{e}{m_i}\nabla_\parallel\phi - \frac{R_{ei\parallel}}{m_i n} - \frac{V_{i\parallel}S_n}{n},$$

(parallel ion momentum) (2)

$$\frac{\partial}{\partial t}\left(V_{e\parallel}-\frac{e}{m_e}A_\parallel\right) = -V_{e\parallel}\nabla_\parallel V_{e\parallel} - \frac{1}{B}\mathbf{b}\times\nabla\phi\cdot\nabla V_{e\parallel} - \frac{\nabla_\parallel p_e}{m_e n} + \frac{e}{m_e}\nabla_\parallel\phi + \frac{R_{ei\parallel}}{m_e n} - \frac{V_{e\parallel}S_n}{n},$$

(Ohm's law) (3)

$$\frac{\partial\Omega}{\partial t} = -\nabla\cdot\left(\frac{1}{B}\mathbf{b}\times\nabla\phi\cdot\nabla\boldsymbol{\omega}\right) - \nabla\cdot\left(\nabla_\parallel\left(V_{i\parallel}\boldsymbol{\omega}\right)\right) + B\nabla_\parallel\left(\frac{J_\parallel}{B}\right) + \nabla\times\left(\frac{\mathbf{b}}{B}\right)\cdot\nabla p_e + \nabla\cdot\left(\mu_\Omega\nabla_\perp\Omega\right),$$

(vorticity) (4)

$$\frac{\partial T_e}{\partial t} = -V_{e\parallel}\nabla_\parallel T_e - \frac{1}{B}\mathbf{b}\times\nabla\phi\cdot\nabla T_e - \frac{2B}{3n}\nabla_\parallel\left(\frac{q_{e\parallel}}{B}\right) + \frac{2T_e}{3en}\nabla\times\left(\frac{\mathbf{b}}{B}\right)\cdot\left(\nabla p_e - en\nabla\phi + \frac{5}{2}n\nabla T_e\right) - \frac{2T_e}{3}B\nabla_\parallel\left(\frac{V_{e\parallel}}{B}\right) + \frac{2}{3}\frac{\left(V_{i\parallel}-V_{e\parallel}\right)}{n}R_{ei\parallel} + \frac{2S_E}{3n} + \frac{V_{e\parallel}^2 S_n}{3m_e n} - \frac{T_e S_n}{n} + \frac{2}{3n}\nabla\cdot\left(\kappa_{e\perp}\nabla_\perp T_e\right).$$

(electron temperature evolution) (5)

The electron density is n, while $V_{i\parallel}$ and $V_{e\parallel}$ are the ion and electron parallel velocities, T_e and $p_e = nT_e$ are the electron temperature and pressure, ϕ and $J_\parallel = en\left(V_{i\parallel} - V_{e\parallel}\right)$ are the electrostatic potential and parallel current, and m_i and m_e are the deuteron and electron masses.

Parallel and perpendicular, denoted by subscripts $\parallel$ and $\perp$, are taken with respect to the total magnetic field, while $\mathbf{b}$ and B are the direction and magnitude of the equilibrium magnetic field, which is taken to be uniform and not evolving. The parallel gradient accounts for the perturbed, parallel magnetic potential $A_\parallel$, such that $\nabla_\parallel = \mathbf{b}\cdot\nabla - B^{-1}\mathbf{b}\times\nabla A_\parallel\cdot\nabla$, but magnetic perturbations are neglected in the perpendicular gradient $\nabla_\perp = \nabla - \mathbf{b}\cdot\nabla$. The system of equations is completed by the parallel component of Ampère's law $-\nabla_\perp^2 A_\parallel = \mu_0 en(V_{i\parallel} - V_{e\parallel})$, where μ_0 is the permeability of free space and e is the proton charge, which is used to calculate $A_\parallel$, $V_{i\parallel}$ and $V_{e\parallel}$ from the quantities evolved in the code, $\chi_i = V_{i\parallel} + eA_\parallel/m_i$ and $\chi_e = V_{e\parallel} - eA_\parallel/m_e$.

The particle and energy sources, represented by S_n and S_E, are used to maintain the background profiles as described in section 3.2, and they do not add parallel momentum to the plasma. The explicit expressions for the parallel friction $R_{ei\parallel} = 0.51 m_e n \left(V_{i\parallel} - V_{e\parallel}\right)/\tau_e - 0.71 n \nabla_\parallel T_e$ and the parallel electron thermal conduction $q_{e\parallel} = -3.16 n T_e \tau_e \nabla_\parallel T_e / m_e - 0.71 n T_e \left(V_{i\parallel} - V_{e\parallel}\right)$ are taken from Braginskii [12] as discussed, where $\tau_e = 12\pi^{3/2} m_e^{1/2} T_e^{3/2} \epsilon_0^2 / 2^{1/2} n e^4 \ln\Lambda$ is the electron collision time and ϵ_0 is the permittivity of free space. The Coulomb logarithm $\ln\Lambda = 12.24$ is calculated [7] using the reference parameters given in Appendix A. The prefactors $D_\perp$, μ_Ω, and $\kappa_{e\perp}$ of the diffusive cross-field terms have previously been taken to vary from the classical collisional limit to an effective value representing the Pfirsch-Schlüter enhancement due to a toroidal magnetic field geometry [47, 48]. The effect of this variation will be discussed further in section 3.3.

The generalised vorticity is $\Omega = \nabla \cdot \boldsymbol{\omega}$, with $\boldsymbol{\omega} = en\nabla_\perp \phi / \Omega_i B$ and the ion gyrofrequency $\Omega_i = eB/m_i$. Previously, in [34], the STORM model was updated to remove the Boussinesq approximation, with the $E \times B$ advection term written following [35, 36] as $-\mathbf{b} \times \nabla\phi \cdot \nabla\Omega / B - \mathbf{b} \times \nabla \left(\left|\mathbf{b} \times \nabla\phi / B\right|^2 / 2\right) \cdot \nabla n / B$. The form in equation (4), from [42], is more convenient when introducing finite ion temperature. Similarly we introduce here parallel advection in the form $-\nabla \cdot \left(\nabla_\parallel \left(V_{i\parallel} \boldsymbol{\omega}\right)\right)$ as also used in [37], instead of the previous $-V_{i\parallel} \nabla_\parallel \Omega$ form in [34], which was focused on perpendicular dynamics. The parallel advection of vorticity is typically small and we have verified numerically that both these changes have a negligible effect on filament motion. Centre-of-mass positions and velocities are changed by less than 1% for the cold ion cases considered in this paper, until the point where the filaments lose their coherence and break up into small-scale turbulent structures; even then the qualitative behaviour is the same, and overall trends of the centre-of-mass position are similar.

We will be modelling filaments moving in the scrape-off layer (SOL), the open field line region between the confined plasma and the machine wall. The boundary conditions in the direction parallel to the magnetic field model the behaviour of the plasma at the entrance to the sheath which exists in front of the divertor target plates, where the quasineutral approximation breaks down. Bohm boundary conditions [52] are applied here. In the cold ion version of STORM these are sonic ion parallel outflow

$$V_{i\parallel,sh} = \pm \sqrt{\frac{T_{e,sh}}{m_i + m_e}}, \tag{6}$$

where subscript 'sh' denotes a quantity evaluated at the sheath entrance, and electron particle and energy outfluxes regulated by the electrostatic potential at the sheath entrance ϕ_{sh}, which is measured relative to the wall,

$$V_{e\parallel,sh} = \pm \sqrt{\frac{m_i T_{e,sh}}{2\pi m_e \left(m_i + m_e\right)}} \exp\left(-\frac{e\phi_{sh}}{T_{e,sh}}\right), \tag{7}$$

$$Q_{e\parallel,sh} = \left(2 - 0.5 \ln\left(\frac{2\pi m_e}{m_i}\right)\right) n_{sh} T_{e,sh} V_{e\parallel,sh}, \tag{8}$$

where $Q_{e\parallel} = q_{e\parallel} + 5 p_e V_{e\parallel}/2 + m_e n V_{e\parallel}^3/2$ is the electron parallel energy flux.

The basic filament propagation regimes can be understood from equation (4), by recognising that the pressure gradient term on the right of equation (4) represents the charge separation due to drifts in a non-uniform magnetic field. The resulting electric field can then be dominantly balanced by the loss of charge to the sheath, through the $J_\parallel$ term, or via the inertia, through the polarisation term appearing on the left hand side of the equation.

2.2. Hot ion model

We have modified the STORM system defined above in section 2.1 to include the following hot ion effects and looked, step-by-step, for their effect on filament motion.

The parallel projection of the ion stress tensor enters the ion parallel velocity equation, introducing primarily the effect of the parallel ion pressure gradient to the right of equation (2), $-\nabla_\parallel p_i/m_i n$, where $p_i = nT_i$ is the ion pressure and T_i is the ion temperature. For this short study we have retained only the standard uniform magnetic field expression for the collisionless viscosity, [12, 42], whose parallel projection is $\mathbf{b}\cdot(\nabla\cdot\pi^{\rm gy}) \approx -m_i n \mathbf{V}_d\cdot\nabla V_{i\parallel}$, with $\mathbf{V}_d = \mathbf{b}\times\nabla p_i/m_i n\Omega_i$ the ion diamagnetic velocity. This produces simply a diamagnetic cancellation, so no advection by the diamagnetic flow enters the second term on the right hand side of equation (2). Finally we keep the simple contribution from the parallel collisional viscosity, $-2B^{3/2}\nabla_\parallel\left(\pi_{ci}/B^{3/2}\right)/3m_i n$, where $\pi_{ci} = -2\eta_i B^{-1/2}\nabla_\parallel\left(B^{1/2}V_{i\parallel}\right)$, $\eta_i = 0.96 p_i\tau_i$ and $\tau_i = 2^{1/2}(m_i/m_e)^{1/2}(T_i/T_e)^{3/2}\tau_e$, neglecting for simplicity the corrections in the drift regime driven by the parallel heat flux gradients [40, 41]. (The comparison to the form retained in [37] can be made readily using equations A1, and B1, B2, B8 of [42].) These common simplifications of the contribution of the stress tensor could be motivated as filaments occur at the cool plasma edge, so at large aspect ratio on many tokamaks. Then geometric corrections to these terms may have a weak effect, but this remains to be validated by comparisons to simulations of more complete systems.

The enhancement of the basic drive term by the ion pressure appears on the right of equation (4) as $\nabla\times(\mathbf{b}/B)\cdot\nabla p_i$. The ion diamagnetic flow, through the ion polarisation, now enters the definition of the generalised vorticity $\Omega = \nabla\cdot\boldsymbol{\omega}$ as $\boldsymbol{\omega} = \left(en\nabla_\perp\phi + \nabla_\perp p_i\right)/\Omega_i B$. The contribution of the ion stress tensor cancels the advection by the diamagnetic flow and introduces only the collisional viscous term, $\nabla\times(\mathbf{b}/B)\cdot\nabla\pi_{ci}/6$, to the right of equation (4), as is used in [37].

With the set of equations described so far we can study the effects of isothermal hot ions. Remembering that introducing electron temperature variation within filaments had a tendency to slow their radial motion [31], we will also go on to consider how the effects of the terms described so far are altered upon including ion temperature evolution. We use an equation analogous to that for the electron temperature evolution,

$$\begin{aligned}\frac{\partial T_i}{\partial t} = & -V_{i\parallel}\nabla_\parallel T_i - \frac{1}{B}\mathbf{b}\times\nabla\phi\cdot\nabla T_i - \frac{2B}{3n}\nabla_\parallel\left(\frac{q_{i\parallel}}{B}\right)\\ & + \frac{2T_i}{3en}\nabla\times\left(\frac{\mathbf{b}}{B}\right)\cdot\left(\nabla p_e - en\nabla\phi - \frac{5}{2}n\nabla T_i\right)\end{aligned}$$

$$- \frac{2}{3} T_i B \nabla_\parallel \left(\frac{V_{e\parallel}}{B} \right) + \frac{2T_i}{3n} \left(V_{i\parallel} - V_{e\parallel} \right) \nabla_\parallel n - \frac{4\pi_{ci}}{9n\sqrt{B}} \nabla_\parallel \left(\sqrt{B} V_{i\parallel} \right)$$
$$+ \frac{2Q_i}{3n} + \frac{2S_{Ei}}{3n} + \frac{S_n V_{i\parallel}^2}{3m_i n} - \frac{T_i S_n}{n} + \frac{2}{3n} \nabla \cdot \left(\kappa_{i\perp} \nabla_\perp T_i \right). \quad (9)$$

Note that this form containing p_e can be understood as following from the general energy conservation moment equation for a species, given for example by the form in equation (2.17) of [7], upon substituting the expression for the compression of the ion polarisation from the plasma force balance equation and neglecting advection by the polarisation velocity compared to its compression. This equation agrees with the conservative form given in [42] on using the electron parallel momentum equation as given in equation (72) of [42], with the simplifications to viscosity and neglect of advection by the polarisation velocity already discussed. The parallel thermal conduction is again taken from Braginskii [12] $q_{i\parallel} = -\kappa_{i\parallel} \nabla_\parallel T_i$ with $\kappa_{i\parallel} = 3.91 n T_i \tau_i / m_i$. When using the ion temperature equation, the collisional energy exchange $Q_i = 3nm_e \left(T_e - T_i \right) / m_i \tau_e$ must also appear on the right of the electron temperature equation (5), with opposite sign, $-2Q_i/3n$. The perpendicular diffusion coefficient for the ion temperature $\kappa_{i\perp}$ is defined in section 4.4, following the discussion of dissipation parameters in section 3.3. Note that the hot ion equations are written out in full, in normalised form, in Appendix A.

The sheath boundary conditions for the ions are modified when taking finite ion temperature into account. The sonic parallel outflow boundary condition includes the finite ion temperature in the sound speed

$$V_{i\parallel,sh} = \pm \sqrt{\frac{T_{e,sh} + T_{i,sh}}{m_i + m_e}}. \quad (10)$$

For simplicity the ion parallel thermal conduction is set to zero at the sheath entrance since advection should dominate, with the ions flowing as fast as their thermal speed due to the sonic boundary condition. The electron sheath boundary conditions are not modified.

A similar system to that defined here was implemented in the GBS code and used to study the effect of hot ions on electrostatic turbulence, identifying relevant linear instabilities from the system dispersion relation [38]. For ease of comparison we give the electromagnetic dispersion relation of our system in the isothermal limit, linearising the set of hot ion equations with $\partial_t \to -i\omega$ and $\nabla \to i\mathbf{k}$,

$$\omega^2 \left(1 + \frac{k_\perp^2 c^2}{\omega_{pe}^2} \frac{1}{\left(1 + \frac{m_e}{m_i} \right)} \right) + i\omega \frac{0.51 m_e}{n e^2 \tau_e} \frac{k_\perp^2}{\mu_0} \left(1 - \frac{k_\parallel^2 c_{sm}^2}{\omega^2} \right)$$
$$= k_\parallel^2 V_A^2 \left[1 + k_\perp^2 \rho_{sm}^2 + \frac{k_\parallel^2 c_{sm}^2}{\omega^2} \left(\frac{\omega^2}{k_\parallel^2 V_A^2} - 1 \right) \right]. \quad (11)$$

The Alfvén speed is given by $V_A = B/\sqrt{\mu_0 m_i n}$ and the plasma skin depth is c/ω_{pe}, with c the speed of light in vacuum and $\omega_{pe} = \sqrt{ne^2/\epsilon_0 m_e}$ the plasma frequency. For convenience we define the electron mass corrected sound speed $c_{sm}^2 =$

$(T_i + T_e) / (m_i + m_e)$ and hybrid gyroradius $\rho_{sm} = c_{sm}/\Omega_i$. Taking the cold plasma limit of this expression, neglecting dissipation due to collisions (resistivity), gives the electromagnetic mode $\omega^2 k_\perp^2 m_e + \Omega_i^2 k_\parallel^2 m_i \left(1 + m_e/m_i\right) \left(\omega^2/k_\parallel^2 V_A^2 - 1\right) = 0$, which reduces to $\omega^2 = \Omega_i^2 m_i \left(1 + m_e/m_i\right) k_\parallel^2 / m_e k_\perp^2$ in the electrostatic limit. The latter is the source of the timestep limitation when running in electrostatic mode noted in the introduction to this section, discussed previously for various gyrokinetic codes [54, 55].

3. Numerical method and cold ion reference case

In this section we first briefly outline relevant numerical details, then present for later comparison the typical filament motion produced by the cold ion STORM model, for edge plasma parameters consistent with MAST (examples can also be seen in previous studies such as [48, 31, 34]).

3.1. Numerical method

Here we outline the basic numerical method, which is implemented using the BOUT++ framework [29, 30]. Fuller details will be presented in [43]. The system of equations is normalised to ensure a more stable numerical solution and logarithms of density and temperatures are evolved to ensure positivity. The normalisations and full system of normalised equations are given in Appendix A. The spatial discretisation is finite-difference, using a staggered grid in the parallel direction for velocities and fluxes. An Arakawa stencil is used for $E \times B$ advection terms, except the $E \times B$ advection in the non-Boussinesq vorticity equation (first term on the right hand side of (4)). For that, inspired by a scheme used in Grillix [53], ϕ and $\boldsymbol{\omega}$ are interpolated to cell faces in the perpendicular plane, an Arakawa bracket operator is used on the cell-face points to calculate the advection of the vector components of $\boldsymbol{\omega}$, and staggered derivatives are then taken to calculate the divergence on the cell-centre grid. For parallel advection terms a second-order accurate upwind scheme is used, and the remaining derivatives are taken with a second-order centred discretisation. The spatial grid used here has $240 \times 64 \times 128$ points in the radial, parallel and binormal directions, and a size, in terms of the representative ion sound radius $\rho_{s0} = 1.29\,\mathrm{mm}$, of $L_\mathrm{radial} \times L_\parallel \times L_\mathrm{binormal} = 93.75\rho_{s0} \times 11000\rho_{s0} \times 50\rho_{s0} = 12.1\,\mathrm{cm} \times 14.2\,\mathrm{m} \times 6.44\,\mathrm{cm}$, giving a perpendicular grid spacing of $0.391\rho_{s0} = 0.503\,\mathrm{mm}$ and a parallel grid spacing of $172\rho_{s0} = 0.221\,\mathrm{m}$. The inversion to calculate electrostatic potential ϕ from the generalised vorticity Ω and also the inversion for electron velocity $V_{e\parallel}$, ion velocity $V_{i\parallel}$, and magnetic potential $A_\parallel$ from the combined variables χ_e and χ_i through Ampère's law, are solved with a multigrid-preconditioned Krylov iterative scheme. The method of lines is used to separate the time discretisation from the spatial discretisation just described, and the CVODE matrix-free, adaptive-order, adaptive-step Newton-Krylov implicit solver from the SUNDIALS suite [44] is used as the time-solver.

3.2. Initialisation

The domain considered is a simplified representation of the region beyond the separatrix of a double-null diverted tokamak configuration, with sheath boundary conditions representing divertor target plates at either end of the field lines. The simulations are performed in a slab magnetic field geometry, with a constant, uniform magnetic field $B = 0.5\,\mathrm{T}$. The effect of non-uniform magnetic field is retained only through the curvature terms, representing a magnetic field having purely radial curvature [45] $\nabla \times (\mathbf{b}/B) \cdot \nabla = 2\left(BR_c\right)^{-1} \nabla_z$, with radius of curvature $R_c = 1.5\,\mathrm{m}$. The x-coordinate represents the radial direction, y is along the field line, and z is a binormal coordinate, with the origin of the coordinates taken at the centre of the initial filament.

The particle, and electron and ion energy sources, S_n, S_E and S_{Ei}, are used to maintain a time-independent background plasma that varies only in the parallel direction. The density and electron energy sources use forms consistent with previous STORM publications. The particle source is localised near the targets, roughly representing recycling, $S_n = S_{n0}\left[\exp\left(20\left(y/L_\parallel - 1/2\right)\right) + \exp\left(-20\left(y/L_\parallel + 1/2\right)\right)\right]$ and the energy sources are localised around the mid-point, representing power loss into the SOL, $S_E = S_{E0}\exp\left(-10\left|y\right|/L_\parallel\right)$ and $S_{Ei} = S_{Ei0}\exp\left(-\left(2y/L_\parallel\right)^2\right)$. The background plasma is taken to have no perpendicular gradients, as usual in seeded filament simulations. It is created by running a 1D simulation, with variation only in the parallel direction, until a steady state is reached where the sources are balanced by losses to the sheaths. The constant prefactors of the sources are tuned for each case studied so that the density and temperatures of the background plasma n_{bg}, $T_{e,\mathrm{bg}}$, and $T_{i,\mathrm{bg}}$ are equal at the midpoint to chosen reference values (see also Appendix A), representative of an L-mode SOL in MAST: $n_{\mathrm{bg}}(y=0) \approx 8\times10^{18}\,\mathrm{m}^{-3}$, $T_{e,\mathrm{bg}}(y=0) \approx 20\,\mathrm{eV}$ and $T_{i,\mathrm{bg}}(y=0) \approx 20\,\mathrm{eV}$. The resulting cold ion background profiles are typical of those used in previous STORM filament studies, and are shown in section 4.1, where the changes introduced by the hot ion terms are discussed.

Filaments are most likely to impact the first wall when their width is at the transition between inertial and sheath-limited regimes, as these filaments have the highest speeds and are also expected to be most stable [46, 8]. Dimensional analysis in the cold ion limit estimates the filament width for this transition to be $\delta_* = \rho_s\left(L_c^2/\rho_s R_c\right)^{1/5}$, with $L_c = L_\parallel/2$ being the connection length [46, 8]. For our parameters, $\delta_* \approx 7.6\rho_{s0} \approx 9.83\mathrm{mm}$ and we therefore take the initial filament width to be $\delta_\perp = 5\rho_{s0} \approx 6.44\mathrm{mm}$, representative of this characteristic scale. The filament is initialised on top of the background by adding

$$\Delta_a = A_a \frac{1}{2}\left[1 - \tanh\left(\frac{y-\delta_\parallel/2}{L_\parallel/8}\right)\right]\frac{1}{2}\left[1 - \tanh\left(\frac{-y-\delta_\parallel/2}{L_\parallel/8}\right)\right]\exp\left(-\frac{x^2+z^2}{\delta_\perp^2}\right) \quad (12)$$

for $a = n, T_i, T_e$ to the density, ion temperature or electron temperature respectively. All perturbations have $A_n = 2\,n_{\mathrm{bg}}(y=0)$ and, when evolving ion temperature using equation (9), an ion temperature perturbation, set by $\hat{A}_{T_i}$ through $A_{T_i} = \hat{A}_{T_i} T_{i,\mathrm{bg}}(y=0)$. The electron temperature perturbation is set to zero for simplicity, except in section 4.5

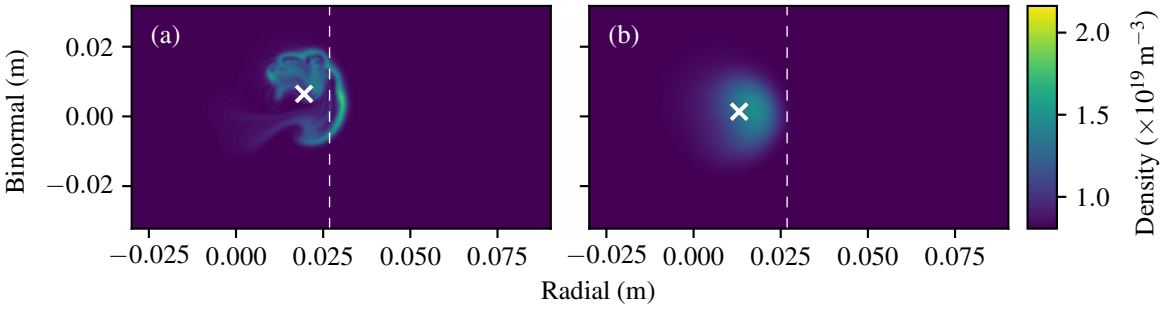

Figure 1. Density at the midplane $y = 0$, 25.9 μs after initialisation for cold ion simulations with (a) classical Braginskii dissipation and (b) dissipation enhanced according to (13), (14), and (15) with $q = 7$. White crosses show the centre of mass of the filament and the vertical dashed line shows the radial position of the centre of mass of the hot, isothermal ion case (figure 4e) for reference.

where the perturbation is set by $\hat{A}_{T_e}$ through $A_{T_e} = \hat{A}_{T_e} T_{e,\mathrm{bg}}(y = 0)$. The initial parallel extent $\delta_\parallel = L_\parallel/2$ represents filaments born between the X-points of a diverted tokamak and (12) is used everywhere except section 4.3, where an initial perturbation with no parallel variation $\Delta_a = A_a \exp\left(-\left(x^2 + z^2\right)/\delta_\perp^2\right)$ is used for comparison to previous 2D simulations [22].

The perpendicular boundaries of the domain do not represent physical boundaries and are far enough away to have little effect on the isolated filaments considered here, so to constrain the simulation as little as possible, and for numerical convenience, Neumann boundary conditions are used at the radial boundaries, while the binormal direction is taken to be periodic. The exception is the electrostatic potential ϕ, which uses a Dirichlet radial boundary condition set equal to the background value, which is set by parallel force balance on the electrons.

3.3. Cold ion reference case

In the cold ion limit initialised filaments move radially across the domain, showing the well-known mushrooming behaviour, see for example [46, 13], with the density piling up into a steep front at the leading edge of the filament. A snapshot of the density is shown in figure 1a, at a time $t = 25.9\,\mu\mathrm{s} = 0.114\,L_c/c_{s0}$, common to all the snapshots shown, when the filaments in all the simulations have evolved significantly but have not yet broken up. Here c_{s0} is a characteristic sound speed defined in Appendix A. The scale of the structures formed is $\sim 1.8\,\mathrm{mm}$, which is comparable to an ion gyroradius at characteristic ion temperatures of 20 eV. In a tokamak SOL the ion temperature is typically found to be greater than the electron temperature [9, 10, 11], and the formation of such fine structure would be prevented by the averaging effect of ion Larmor orbits. Increasing the perpendicular diffusion and viscosity can smooth out the gyro-scale structure in the simulations. (This is illustrated in figure 1b, discussed at the end of this section.) The coefficients used in STORM for perpendicular diffusion and

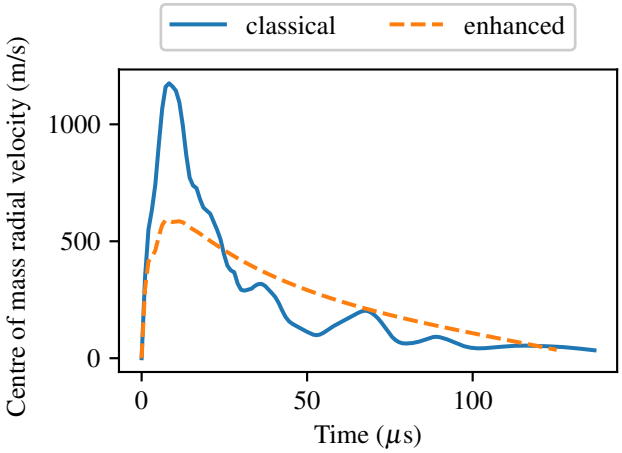

Figure 2. Radial velocity of the filament centre of mass for cold ion simulations with classical Braginskii dissipation (solid blue) and dissipation enhanced according to (13), (14), (15) with $q = 7$ (dashed orange).

viscosity are based on classical collisional values, with a prefactor introduced in [47], motivated as extrapolating neoclassical Pfirsch-Schlüter transport coefficients into the SOL in the absence of a rigorous derivation. The coefficient used for ambipolar particle diffusion due to ion-electron friction is

$$D_\perp = \left(1 + 1.3q^2\right)\left(1 + T_i/T_e\right) T_e/m_e\Omega_e^2\tau_e, \tag{13}$$

where $\Omega_e = eB/m_e$ is the electron gyrofrequency, for the perpendicular viscosity which provides damping in the generalised vorticity equation

$$\mu_\Omega = \left(1 + 1.6q^2\right) 3T_i/4m_i\Omega_i^2\tau_i, \tag{14}$$

and for the perpendicular diffusion of electron energy

$$\kappa_{e\perp} = \left(1 + 1.6q^2\right) 4.66nT_e/m_e\Omega_e^2\tau_e. \tag{15}$$

These expressions have previously been used in STORM assuming $T_i = T_e$ (although the rest of the model assumed cold ions) and we continue to evaluate them the same way for convenience. In this paper we set the 'safety factor' $q = 0$, reducing these coefficients to the classical perpendicular collisional transport coefficients of Braginskii [12], apart from the cases shown in figures 1b and 4b which have $q = 7$ for comparison to previous work. The classical values are small and are retained mainly to ensure numerical stability. Although the prefactors were originally motivated as neoclassical values extrapolated into the SOL, we could also interpret the enhancement as a way to suppress small-scale structure in the absence of finite ion temperature effects, with q a free parameter used to control the size of the dissipation. Several previous papers have used $q = 7$ [48, 31, 32], for which these prefactors give two orders of magnitude enhancement of the perpendicular diffusion, viscosity and thermal conduction. Militello et al. [49] used a slightly smaller $q = 4.8$ and found reasonable agreement with experimental measurements of SOL filament velocity from MAST.

The effect of the enhanced dissipation coefficients on the filament motion is demonstrated in figure 1b. In contrast to the classical dissipation filament, figure 1a, which is already strongly mushroomed and breaks up shortly after the time shown, the enhanced dissipation filament is still coherent and remains so until its amplitude drops to zero due to parallel losses and perpendicular diffusion. The enhanced dissipation filament moves radially more slowly than the classical dissipation filament, as shown by the radial velocity of the centres of mass in figure 2, consistent with the increased perpendicular viscosity, although at later times the classical dissipation filament slows down as it breaks up.

4. Hot ion filament behaviour

We build an understanding of the effect of hot ions in a series of simulations, introducing the terms discussed in section 2.2. We consider the effect of the terms both qualitatively, by snapshots of the evolution of the filament structure taken at the same time (25.9 μs) for all simulations, at a point well into the evolution of the filaments but before they begin to fragment, and quantitatively, by assessing the time evolution of the number of particles crossing a location 5 cm from the initialisation position of the centre of the filament. This choice was made as representative of the plasma-wall distance – in MAST, which has a remote wall, this is the distance at the midplane from the separatrix to the shadow of the poloidal field coil casing. We begin with the terms in the ion parallel momentum equation and their effect on the background plasma in section 4.1, before comparing the various new terms in the vorticity equation in section 4.2 with an isothermal ion model. After a brief digression in section 4.3 to discuss filaments initialised target to target, to connect the results so far to typical 2D blob simulations, we present results using the full model including ion temperature evolution in section 4.4. In section 4.5 we briefly discuss the impact of including in addition an initial electron temperature perturbation.

4.1. Background plasma and baseline simulation

The background plasma, set as described in section 3.2, is significantly affected by the addition of ion temperature. In figure 3 we compare the parallel background profiles of density, temperature and parallel velocity (equal for electrons and ions in the background plasma) in the reference cold ion case to those allowing for isothermal hot ions, or evolving ion temperature. The introduction of non-zero ion viscosity in the ion parallel momentum equation has an influence due to the very strong gradients in the ion parallel velocity near the sheaths, and causes the density to peak much more strongly near the targets. When in addition the ion temperature is allowed to evolve, there is a parallel gradient of the ion temperature. Upstream of the particle source there is no particle flux and therefore no parallel flow, so the total parallel momentum equation makes the total pressure constant in this region. Therefore the decreasing ion temperature requires an

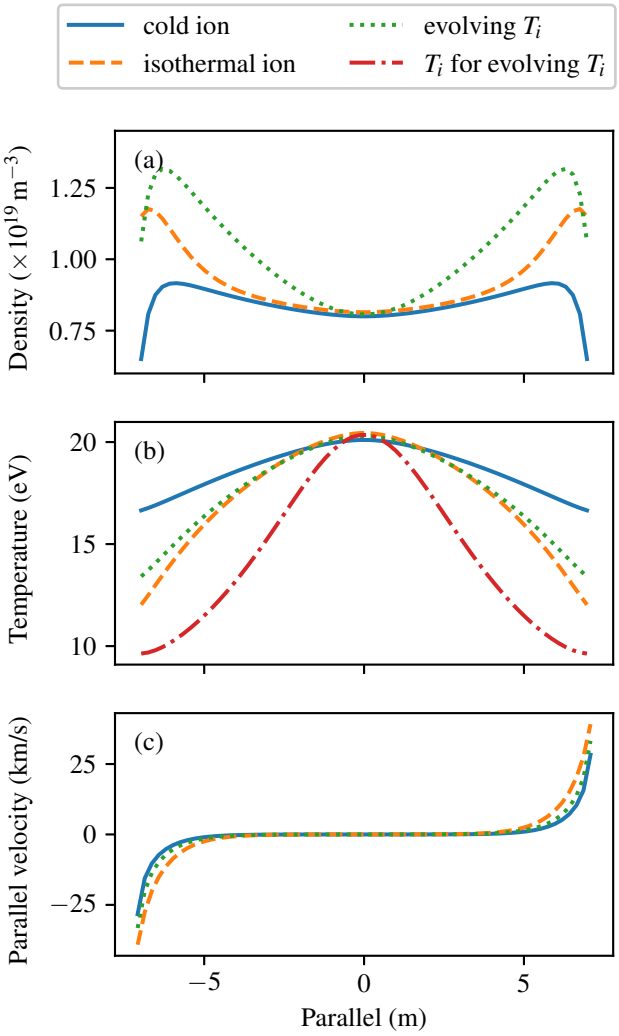

Figure 3. Variation of the background plasma in the parallel direction. For cold ion (solid blue), isothermal ions (dashed orange) and evolving ion temperature (dotted green) cases (a) density; (b) electron temperature; and (c) parallel velocity (equal for ions and electrons in the background plasma) are shown. The ion temperature in the evolving ion temperature case is also shown in (b) by the dash-dotted red line.

increasing density to compensate.

The differences just described in the background plasma affect the radial propagation of filaments. Linearising the boundary conditions (10) and (7) around the floating potential gives the sheath current flowing in response to the potential perturbation $\delta\phi_{sh}$ as

$$\delta J_{\parallel,sh} = \frac{e^2 n_{sh}}{T_{e,sh}} \left(\frac{T_{e,sh} + T_{i,sh}}{m_i + m_e} \right)^{1/2} \delta\phi_{sh}, \tag{16}$$

so the lower density, higher electron temperature and zero ion temperature in the cold ion case all result in a weaker sheath current in response to a given potential perturbation, draining less of the dipolar potential that generates the radial velocity of the filament. In figure 4a, we show a simulation with finite ion temperature terms retained only in

the parallel ion momentum equation, so the background plasma is the 'isothermal ion' case of figure 3. The parallel expansion of the filaments considered in this paper is small during the period when they have the fastest radial velocities, so the effect of terms varying due to the filament are secondary compared to the effect of the background plasma. This simulation is thus representative of the cold ion perpendicular dynamics in the modified background, and we do indeed see that the radial propagation of the filament is slower in this case than in figure 1a. Figure 4b demonstrates the same effect at the higher dissipation parameters of figure 1b. In the following section, we therefore take the case shown in figure 4a, rather than figure 1a, as the baseline for comparison.

4.2. Isothermal hot ion filaments

In this subsection we analyse the effect of the terms in the isothermal hot ion model defined in section 2.2 on the filament motion, comparing to the baseline case representative of cold ion perpendicular dynamics with the 'isothermal ion' background plasma introduced in section 4.1 and shown in figure 4a.

When only the ion temperature contribution to the curvature drive term in the vorticity equation is included (figure 4c), the speed of the filament is increased, as may be expected. The mushrooming behaviour and subsequent break up into smaller structures are also accelerated.

Adding instead only the ion pressure term in the generalised vorticity, to give $\boldsymbol{\omega} = (en\nabla_\perp\phi + \nabla_\perp p_i)/\Omega_i B$, reduces the mushrooming of the filament (figure 4d), which remains more coherent than in the baseline figure 4a, although the filament in this case still breaks apart soon after the time shown. This ion pressure term appears to act as an effective sink in the vorticity equation, suppressing the formation of the small-scale structure that causes mushrooming. The radial velocity remains similar to the baseline.

With the full set of isothermal, finite ion temperature terms, the filament is both more coherent and faster than the baseline case (figure 4e). The peak velocity for this case is slightly lower than the filament with only the drive term included, but the velocity is sustained for longer, leading eventually to a larger radial displacement of the centre of mass.

To assess the potential importance of the effects just discussed for particle transport to the far SOL, we examine the number of particles that have passed $x = 5\,\mathrm{cm}$. 5 cm is representative of the distance from the separatrix to the wall shadow at the outboard midplane in MAST [49]. We calculate the total number of particles by integrating the flux across the surface at 5 cm, shown in figure 5 as a fraction of the initial number of particles in the seeded filament (which is the same for all cases considered here),

$$F_{>5\,\mathrm{cm}}(t) = \frac{\int_{t'=0}^{t'=t} \left(n(t',x,y,z)\, V_{e,x}(t',x,y,z)\right)\big|_{x=5\,\mathrm{cm}}\, dt'\, dy\, dz}{\int \left(n(t=0,x,y,z) - n_{\mathrm{bg}}(y)\right) dx\, dy\, dz}, \tag{17}$$

where $V_{e,x}(t,x,y,z)$ is the total radial velocity of the electrons. The baseline plus

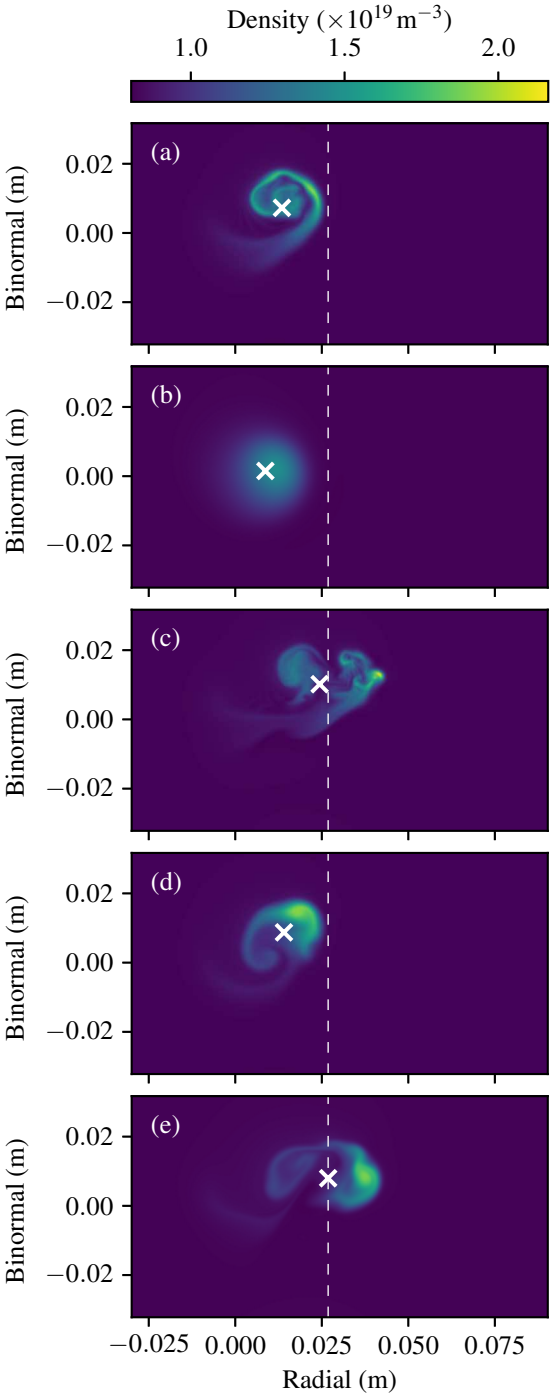

Figure 4. Density snapshots at the midplane of the simulation, at $t = 25.9\mu$s. The baseline case including only the isothermal ion temperature terms in the ion parallel momentum equation is shown with (a) classical perpendicular dissipation and (b) enhanced perpendicular dissipation ($q = 7$). The following panels show snapshots additionally retaining (c) the hot ion curvature drive term in the vorticity equation, (d) $\nabla_\perp p_i$ in $\boldsymbol{\omega}$, and (e) all isothermal hot ion terms. White crosses show the centre of mass; vertical dashed line shows the radial position of the centre of mass of the full isothermal case (e) for reference.

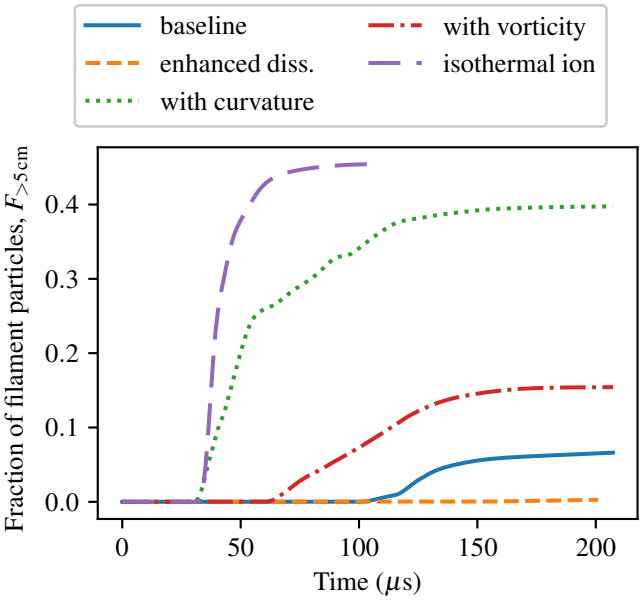

Figure 5. Number of particles from a filament that have crossed the plane 5 cm radially from the initial position of the filament $F_{>5\,\mathrm{cm}}$, measured as a fraction of the total number of particles in the initial filament. Cases shown are the baseline (solid blue) with ion temperature terms included only in the ion parallel momentum equation; baseline plus enhanced dissipation (dashed orange); baseline plus hot ion curvature drive term in the vorticity equation (dotted green); baseline plus $\nabla_\perp p_i$ term in $\boldsymbol{\omega}$ (dash-dotted red); and the case with all isothermal-ion terms (wide-dashed purple).

enhanced dissipation case (figure 4b) remains coherent but diffuses away and slows down quickly enough that a negligible number of particles ever reach $x = 5\,\mathrm{cm}$. The filaments in all the other cases have fragmented by the time they reach $x = 5\,\mathrm{cm}$, but the filament in the simulation with the full set of isothermal ion terms (figure 4e) fragments the least, with a relatively large, coherent filament reaching $x > 5\,\mathrm{cm}$; this gives the sharp rise in number of particles seen in figure 5 and leads to the largest number of particles crossing $x = 5\,\mathrm{cm}$. The filament retaining only the enhanced drive (figure 4c) travels quickly, as expected, but breaks up into several smaller filaments, so the first particles arrive at the same time as those in the full isothermal case, but the rise is less steep as other fragments arrive later, and fewer particles in total reach $x = 5\,\mathrm{cm}$. The behaviour of the baseline (figure 4a) and the case with the modified vorticity but no additional drive (figure 4d) are similar, as may be expected from the discussion above. The filaments break up and lose most of their particles to parallel flux through the sheath before reaching $x > 5\,\mathrm{cm}$, with the first particles arriving significantly later than in the cases with enhanced drive, the rise in particle number being less steep and the total number of particles arriving being much smaller.

There is a threshold energy for sputtering of wall material by plasma ions, so ion energy transport to the far SOL is an important topic. However, the simplified setup in this paper does not give a representative picture of the energy transport. For isothermal

ions the energy per ion is a constant, so ion energy is just transported with the particles, while even with evolving ion temperature (section 4.4) the radially constant background plasma means the filaments can never drop below 20 eV. We have therefore chosen to focus on the particle transport by filaments.

4.3. Target to target filaments

In this subsection we consider filaments initialised with perturbations that stretch the full distance from target to target, using an initial perturbation with no parallel variation $\Delta_a = A_a \exp\left(-\left(x^2 + z^2\right)/\delta_\perp^2\right)$, as noted in section 3.2. This choice minimises parallel gradients so that spin due to the adiabatic parallel electron response is mostly eliminated. Note that as the amplitude is kept fixed, the filaments in these cases have twice the total number of particles as those in the rest of the paper. These filaments most closely resemble those simulated in 2D codes which assume closures for the parallel dynamics. Target to target filament simulations corresponding to those shown in figure 4, panels (a)-(e) – the baseline case, enhanced perpendicular dissipation, additional curvature drive from finite T_i, T_i-modified vorticity, and the full isothermal model – are shown in figure 6, panels (a)-(e). The structures in figure 6 are much closer to the up-down symmetry typical of 2D simulations than the corresponding cases with parallel gradients in figure 4 and do indeed travel further, as expected from the reduced spinning and increased drive due to increased total number of particles. They also transport a larger fraction of the particles past $x = 5\,\mathrm{cm}$ (not shown) - apparently for these cases the increased coherence and drive of the filaments is more significant for the particle transport than the increase in parallel losses due to the filaments being initialised attached to the targets. The target to target filament in the full isothermal ion temperature case, figure 6e, is similar in appearance to those reported in [22] using an isothermal, 2D, hot ion, gyrofluid model. The figures shown in [22] used a large ion to electron temperature ratio $T_i/T_e = 3$ or 7, which is likely the cause of the increased poloidal motion of those filaments compared to figure 6e.

4.4. Hot ion filaments with evolving ion temperature

This subsection considers the full hot ion model including the evolving ion temperature by adding equation (9), and examines the filament behaviour in comparison to the cold ion and isothermal ion models. We show two simulations using the evolving ion temperature model, the first has no initial ion temperature perturbation $\hat{A}_{T_i} = 0$ and the second introduces an ion temperature perturbation with $\hat{A}_{T_i} = 1$, in addition to the density perturbation.

The ion perpendicular thermal conduction coefficient is treated similarly to the other perpendicular dissipation coefficients discussed in section 3.3. We use $\kappa_{i\perp} = \left(1 + 1.6q^2\right) 2nT_i/m_i\Omega_i^2\tau_i$ from [47] and as in the isothermal ion case take $q = 0$ in all cases in this subsection, so that the ion perpendicular thermal conduction is given by the classical expression of Braginskii [12]. Since this coefficient is only used in the ion

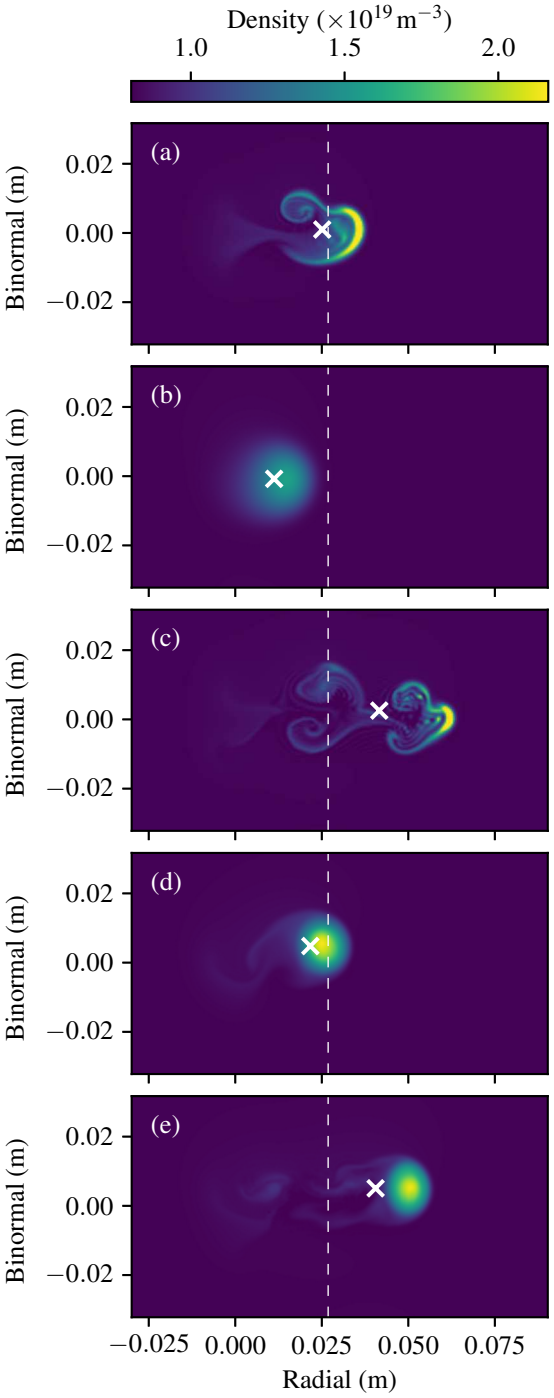

Figure 6. Density snapshots at the midplane of the simulation, at $t = 25.9\mu$s, for filaments initialised target to target. The baseline case including only the isothermal ion temperature terms in the ion parallel momentum equation is shown with (a) classical perpendicular dissipation and (b) enhanced perpendicular dissipation ($q = 7$). The following panels show snapshots additionally retaining (c) the hot ion curvature drive term in the vorticity equation, (d) $\nabla_\perp p_i$ in $\boldsymbol{\omega}$, and (e) all isothermal hot ion terms. White crosses show the centre of mass; vertical dashed line shows the radial position of the centre of mass of the standard isothermal case (figure 4e) for reference.

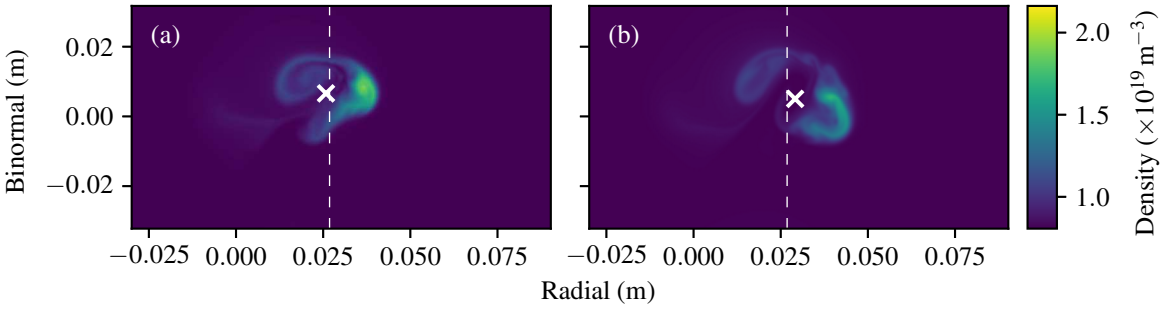

Figure 7. Density at the midplane at $t = 25.9\mu$s for simulations including ion temperature evolution: (a) without ($\hat{A}_{T_i} = 0$) and (b) with ($\hat{A}_{T_i} = 1$) initial ion temperature perturbation. White crosses show the centre of mass of the filament and the vertical dashed line shows the radial position of the centre of mass of the isothermal case (figure 4e) for reference.

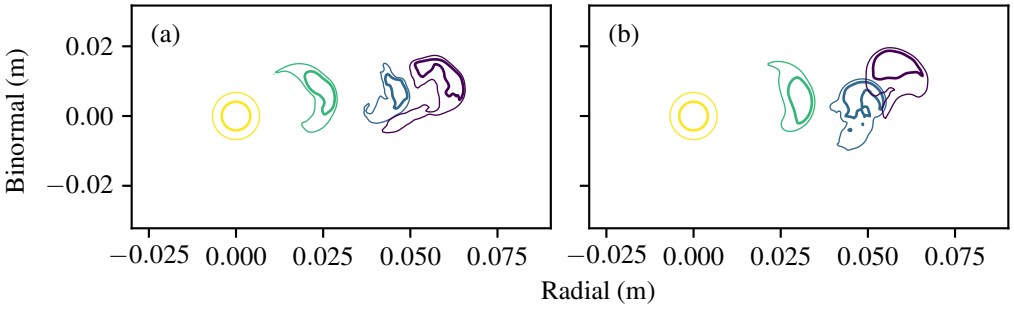

Figure 8. Contours showing 2/3 (thick lines) and 1/3 (thin lines) of the maximum density at several times from 0 (yellow) to 50 μs (purple) for the evolving ion temperature case (a) without ($\hat{A}_{T_i} = 0$) and (b) with ($\hat{A}_{T_i} = 1$) an initial ion temperature perturbation.

temperature equation, we do use the evolving ion temperature T_i instead of evaluating it with $T_i = T_e$.

In this subsection we use the consistent background plasma 'evolving T_i' of figure 3. Note that the differences in density and electron temperature at the sheath entrance are small between the isothermal ion and evolving ion temperature cases, and so the change from the isothermal ion background plasma has a relatively small effect, as discussed in section 4.1. As might be expected, the case with evolving ion temperature but no initial ion temperature perturbation, figure 7a, and the isothermal ion case, figure 4e, are very similar. There are no mechanisms to generate large ion temperature perturbations during the evolution of the filament, and indeed we also observe that ion temperature fluctuations are less than ± 5 eV through the whole simulation. The trajectories of the centres of mass (not shown) of the isothermal ion filament and evolving ion temperature filament without initial ion temperature perturbation are also very similar, the radial position of the centres of mass differs by less than 1.5 mm throughout the simulations.

Adding an initial ion temperature perturbation $\hat{A}_{T_i} = 1$ increases the pressure gradient in the curvature drive term and so would be expected to increase the centre

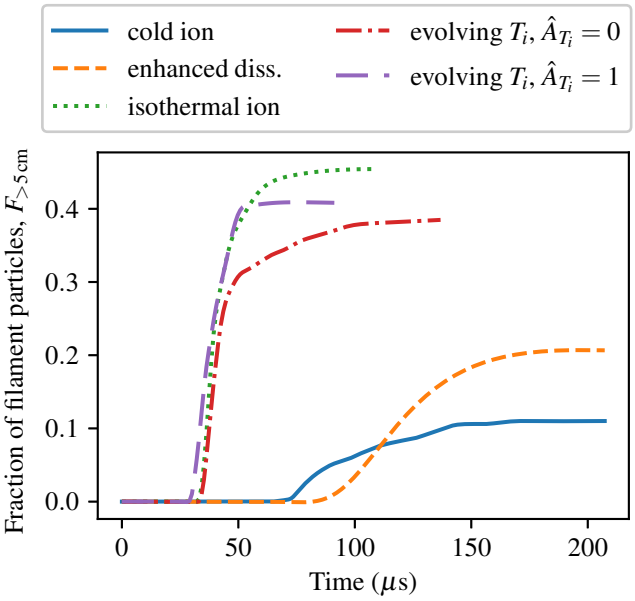

Figure 9. Number of particles from a filament that have crossed the plane 5 cm radially from the initial position of the filament $F_{>5\,\mathrm{cm}}$, measured as a fraction of the total number of particles in the initial filament. Cases shown are cold ion (solid blue); cold ion with enhanced perpendicular dissipation (dashed orange, $q = 7$); isothermal ion (dotted green); and evolving ion temperature without (dash-dotted red, $\hat{A}_{T_i} = 0$) and with (wide-dashed purple, $\hat{A}_{T_i} = 1$) ion temperature perturbation.

of mass radial velocity. The simulation does show an increase in the early stages of the filament motion, up to $t = 18\,\mu$s, compared to the case without an initial ion temperature perturbation. However the ion temperature perturbation also increases the parallel losses by enhancing $\nabla_\parallel p_i$, which accelerates the ion parallel flow and leads to a more rapid drop of the peak density, which in turn decreases the curvature drive and hence the radial velocity, so that by the time shown in figure 7b the filament with an initial ion temperature perturbation has not moved much further than the one without.

An initial ion temperature perturbation also enhances the ion pressure gradient where it contributes to $\boldsymbol{\omega} = (en\nabla_\perp\phi + \nabla_\perp p_i)/\Omega_i B$, which provides an effective sink suppressing small scale structure, as discussed for figure 4d. The extra ion pressure would therefore be expected to make the filament more coherent and this does seem to be the case – the filament with an initial ion temperature perturbation does not become as elongated as the filament with no initial ion temperature perturbation, figure 8. The effect here is minor, but is more significant when counteracting the destabilising effect of an initial electron temperature perturbation, see section 4.5.

We examine the particle transport to the far SOL using $F_{>5\,\mathrm{cm}}$ in a similar way to section 4.2, now comparing in figure 9 the cold ion cases with classical and enhanced dissipation of section 3.3, the full isothermal ion case of section 4.2, and evolving ion temperature cases without and with an ion temperature perturbation. Recall that the background plasmas for these cases are different. The cold ion case transports the

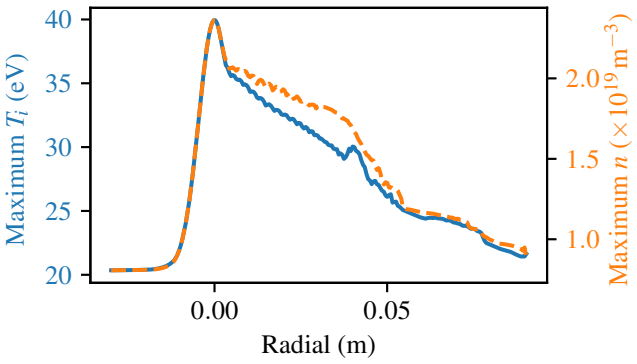

Figure 10. Maximum over the whole duration of the simulation of the ion temperature (solid blue) and density (dashed orange) at each radial position for the case with evolving ion temperature and initialised with an ion temperature perturbation $\hat{A}_{T_i} = 1$.

fewest particles past $x = 5\,\mathrm{cm}$, as it has the smallest drive and least coherent filaments. Enhanced dissipation coefficients make a cold ion filament more coherent, increasing the number of particles transported past $x = 5\,\mathrm{cm}$. However, in comparison to the hot ion cases, the cold ion, enhanced dissipation case has much slower radial motion, allowing more time for parallel losses and the enhanced perpendicular diffusion to remove particles from the filament before it reaches $x = 5\,\mathrm{cm}$, so that the total number of particles transported is about half the number in the hot ion cases. The isothermal ion case transports the most particles past $x = 5\,\mathrm{cm}$, as the additional parallel gradient of ion pressure in the $\hat{A}_{T_i} = 0$ evolving ion temperature case leads to increased particle losses, which are further increased by the ion temperature perturbation in the $\hat{A}_{T_i} = 1$ case. Despite the increased parallel losses, the case with an initial ion temperature perturbation transports more particles past $x = 5\,\mathrm{cm}$ than the case without an initial ion temperature perturbation due to the stronger drive and slightly more coherent structure.

While as noted at the end of section 4.2 the simplified setup here does not give a representative picture of the energy transport, we can observe that the maximum ion temperature that reaches some radial position decreases slightly faster than the maximum density, at least up to $x = 5\,\mathrm{cm}$, figure 10, presenting a direction to be explored in future work.

4.5. Effect of initial electron temperature perturbation

When an initial electron temperature perturbation is imposed $\hat{A}_{T_e} = 1$, the filament spins strongly. As described by Walkden et al. [31], even when the electron temperature perturbation is initially disconnected from the sheaths, rapid parallel thermal conduction of the electrons quickly transports the temperature perturbation to the sheaths. The temperature dependence of the floating potential,

$$\phi_{fl} = \frac{T_e}{2e} \ln\left(\frac{m_i}{2\pi m_e \left(1 + T_{i,sh}/T_{e,sh}\right)}\right), \tag{18}$$

means that the initially monopolar temperature perturbation induces a monopolar

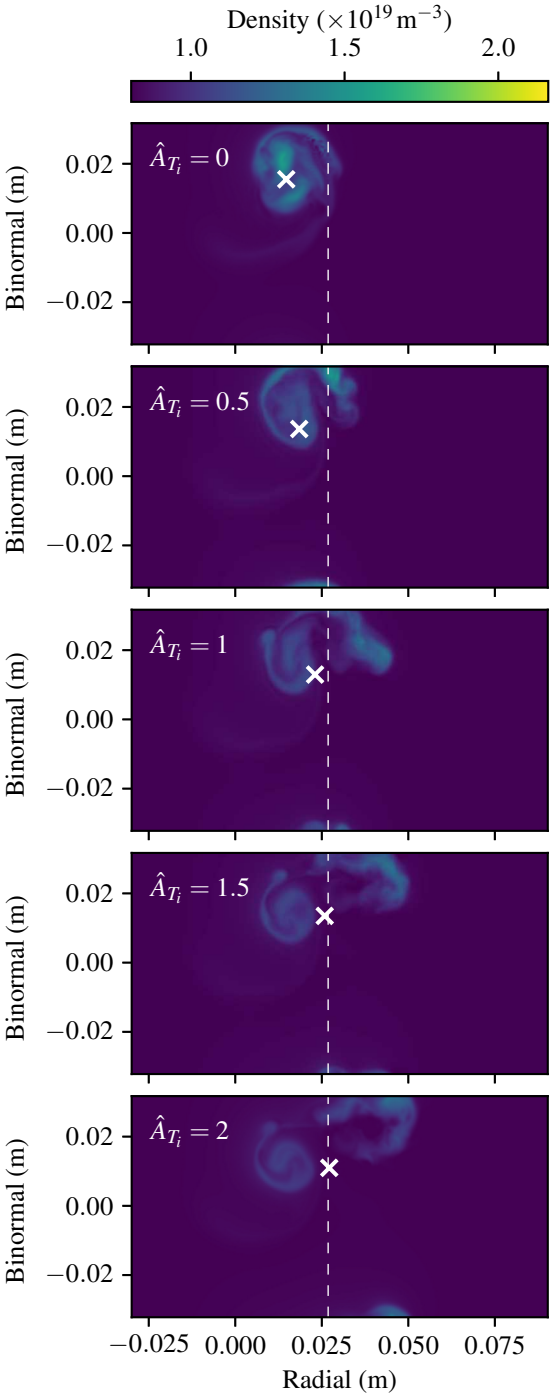

Figure 11. Density snapshots at the midplane of the simulation, at $t = 25.9\,\mu$s for evolving ion temperature cases with an initial electron temperature perturbation $\hat{A}_{T_e} = 1$ for increasing values of the initial ion temperature perturbation $\hat{A}_{T_i}$, as labelled on the panels. White crosses show the centre of mass of the filament and the vertical dashed line shows the radial position of the centre of mass of the isothermal case with no electron temperature perturbation (figure 4e) for reference.

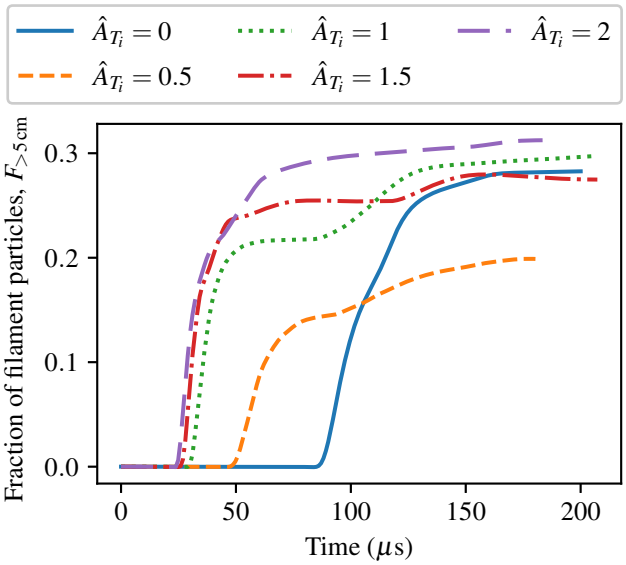

Figure 12. Number of particles from a filament that have crossed the plane 5 cm radially from the initial position of the filament $F_{>5\,\mathrm{cm}}$, measured as a fraction of the total number of particles in the initial filament. Cases shown all have an initial electron temperature perturbation $\hat{A}_{T_e} = 1$ and increasing initial ion temperature perturbations: $\hat{A}_{T_i} = 0$ (solid blue), $\hat{A}_{T_i} = 0.5$ (dashed orange), $\hat{A}_{T_i} = 1$ (dotted green), $\hat{A}_{T_i} = 1.5$ (dash-dotted red), and $\hat{A}_{T_i} = 2$ (wide-dashed purple).

potential variation, giving rise to a circulating $E \times B$ drift that spins the filament around its centre and can strongly inhibit radial motion. The qualitative behaviour is illustrated in figure 11 by snapshots of the filament density for simulations using the full evolving ion temperature model, with an initial electron temperature perturbation $\hat{A}_{T_e} = 1$ and different initial ion temperature perturbations $\hat{A}_{T_i}$.

In the cases with small ion temperature perturbations, $\hat{A}_{T_i} = 0, 0.5$, the filament initially mushrooms, with the density peak moving to the front of the filament. This peak is then stretched out and carried around to the back of the filament by the spin generated by the electron temperature perturbation. Subsequently, the filament partially loses coherence and remains spinning, without significant radial propagation; this is the phase shown in figure 11. Once the electron temperature drops close to the background value due to parallel conduction through the sheaths, the filament forms a potential dipole and begins to move radially again, although rather slowly since its density is now relatively dispersed. This late motion is why a significant number of particles eventually reach $x = 5\,\mathrm{cm}$, as shown in figure 12. In real SOL conditions, it is likely that these very slowly moving, diffuse filaments would be broken up by background turbulence or interaction with other filaments, before they can propagate outwards as they do in the idealised setup here. Cold-ion simulations (not shown) are qualitatively similar to these cases. The partial loss of coherence seen in figure 11 is in contrast to the behaviour reported in Walkden et al. [31], likely due to the use of enhanced dissipation parameters there, as opposed to the classical values used here (see section 3.3).

When the ion temperature perturbation is larger than the electron temperature perturbation, $\hat{A}_{T_i} = 1.5, 2$, the combination of strong drive and spin splits the filament, with most of the mass propagating coherently, leaving behind a diffuse spinning cloud similar to the case with no ion temperature perturbation, see figure 11. The particles in these cases reach $x = 5\,\mathrm{cm}$ (figure 12) at around the same time as in simulations with no initial electron temperature perturbation (figure 9), although there are fewer.

The case with equal initial ion and electron temperature perturbations $\hat{A}_{T_i} = \hat{A}_{T_e} = 1$ shows an intermediate behaviour. A filament does escape without being caught up in the spin, but it is more strongly disrupted than in the cases with $\hat{A}_{T_i} > \hat{A}_{T_e}$ and is slightly delayed in its arrival at $x = 5\,\mathrm{cm}$. This difference is more apparent in animations of the filament evolution (included in supplementary material with the online version of this article) than in the static snapshots shown here.

We also ran a set of simulations (not shown) with a smaller initial electron temperature perturbation $\hat{A}_{T_e} = 0.5$. Similar behaviour was seen, with strong spinning for $\hat{A}_{T_i} = 0$, a coherent filament escaping the spin for $\hat{A}_{T_i} = 1, 1.5, 2$ and intermediate behaviour for $\hat{A}_{T_i} = \hat{A}_{T_e} = 0.5$.

The ion temperature has been observed to be 2-3 times higher in large filaments than in the background during an L-mode discharge on MAST, while the electron temperature of the background was smaller than the ion temperature [9]. Also the electron temperature was not significantly different within the filaments than in the background, consistent with electron temperature being lost rapidly due to parallel conduction. So although we have seen in this section that large electron temperature perturbations could have a drastic impact on the coherence of SOL filaments (when not assuming enhanced dissipation parameters), experimentally these large electron temperature perturbations are not observed. In addition we see from the simulations that coherence can be restored by a significant ion temperature perturbation, of the sort that is observed in experiment. The results of this section are therefore consistent with the standard picture of SOL filaments as coherent objects that can propagate significant distances radially.

5. Summary

Motivated by the experimental observations of significant ion temperature at the outboard midplane of the scrape-off layer, we have investigated here numerically the effect of retaining a description of hot ions in the plasma edge on classic filament propagation. By modifying the STORM plasma edge model, we have considered the effect of the individual hot ion terms, and observed the impact of moving from an isothermal system to one allowing for ion temperature evolution, as was done in previous studies for the electrons [31].

The ion pressure gradient enhances the curvature drive term in the generalised vorticity equation, leading to the increased radial velocity, while the contribution of the ion pressure to the polarisation current acts as an effective sink which suppresses

small scale structure in the vorticity, leading to more coherent filaments. The parallel gradient of the ion pressure enters the ion parallel momentum equation, contributing most significantly to the background plasma profiles, resulting in small changes to filament radial velocities, but no qualitative differences.

Past studies have found that adding evolving electron temperature tends to suppress the radial motion of filaments by causing them to spin, and we observe that when using classical collisional dissipation parameters, filaments initialised with an electron temperature perturbation break up rapidly. In contrast, moving from an isothermal ion model to one with evolving ion temperature has a modest effect on filament propagation. An ion temperature perturbation in the filament gives a small increase in coherence and, initially, in the drive but these compete with increased parallel losses driven by the parallel ion pressure gradient. However, when an ion temperature perturbation is added that is larger than the electron temperature perturbation, it prevents the break up driven by the electron temperature perturbation; this is the experimentally relevant case, as can be expected from the large parallel thermal conductivity of electrons relative to ions.

The radial particle flux due to each filament, measured by the integrated flux of particles crossing the plane 5 cm radially outside the initial centre of the filament, supports these conclusions. Increased coherence or radial velocity of filaments lead to larger particle transport. We leave further investigation of filament energy transport for future work using turbulent simulations with self-consistent radial profiles.

Filaments initialised 'target to target' with minimal parallel gradients correspond more closely than the other cases presented here to 2D blob simulations, and show a more pronounced increase in coherence produced by hot ion effects, with results very similar to the 2D simulations.

This study forms the basis for a comparison when more complete edge models, such as the description of the ion stress tensor in a non-uniform magnetic field, are available. It has however already given us an insight into the range of effects which can arise, and suggests that hot ion effects may contribute to maintaining the coherent structure of SOL filaments observed in many experiments.

Acknowledgments

The authors would like to acknowledge helpful discussions with Gregor Decristoforo, Nick Walkden, Fabio Riva, and Felix Parra.

This work has been funded by the EPSRC Energy Programme [grant numbers EP/T012250/1 and EP/W006839/1]. To obtain further information on the data and models underlying this paper please contact PublicationsManager@ukaea.uk. The simulations presented were carried out in on the Cineca Marconi supercomputer within the framework of the SOLBOUT3, SOLBOUT4 and SOLBOUT5 projects.

Appendix A. Normalised STORM implementation

In this appendix we give the full set of normalised equations, written in the form implemented in STORM. Density $\hat{n} = n/n_0$, temperatures $\hat{T}_e = T_e/T_0$, $\hat{T}_i = T_i/T_0$ and magnetic field $\hat{B} = B/B_0$ are normalised to the reference values n_0, T_0 and B_0 respectively. Other quantities are normalised to parameters derived from these reference quantities and physical constants as follows: lengths to the hybrid gyro-radius $\rho_{s0} = \sqrt{T_0/m_i}$, so $\hat{\nabla} = \rho_{s0}\nabla$; times to the inverse of the gyro-frequency $\Omega_{i0}^{-1} = (eB_0/m_i)^{-1}$ so $\partial/\partial\hat{t} = \Omega_{i0}^{-1}\partial/\partial t$; velocities to the reference, cold ion sound speed $c_{s0} = \sqrt{T_0/m_i}$ so $\hat{V}_{i\parallel} = V_{i\parallel}/c_{s0}$ and $\hat{V}_{e\parallel} = V_{e\parallel}/c_{s0}$; currents to a reference current en_0c_{s0}; electrostatic potential to T_0/e so $\hat{\phi} = e\phi/T_0$; and magnetic potential is represented by the dimensionless variable $\hat{\psi} = eB_0^2A_\parallel/\mu_0 n_0 T_0 m_i c_{s0}$. In this paper we use the values $n_0 = 8\times10^{18}\mathrm{m}^{-3}$, $T_0 = 20\mathrm{eV}$ and $B_0 = 0.5\mathrm{T}$, which are representative values for the L-mode SOL in MAST [49]. The set of STORM equations is thus

$$\begin{aligned}\frac{\partial\hat{n}}{\partial\hat{t}} = &-\frac{1}{\hat{B}}\mathbf{b}\cdot\hat{\nabla}\hat{\phi}\times\hat{\nabla}\log\hat{n} - \hat{B}\hat{\nabla}_\parallel\left(\frac{\hat{V}_{e\parallel}}{\hat{B}}\right) - \hat{V}_{e\parallel}\hat{\nabla}_\parallel\log\hat{n} + \frac{\hat{S}}{\hat{n}}\\ &+\hat{D}_\perp\frac{\hat{\nabla}_\perp^2\hat{n}}{\hat{n}} + \hat{\nabla}_\perp\hat{D}_\perp\cdot\hat{\nabla}_\perp\log\hat{n}\\ &-\hat{\nabla}\times\left(\frac{\mathbf{b}}{\hat{B}}\right)\cdot\hat{\nabla}\hat{\phi} + \frac{\hat{T}_e}{\hat{n}}\hat{\nabla}\times\left(\frac{\mathbf{b}}{\hat{B}}\right)\cdot\hat{\nabla}\hat{n} + \hat{\nabla}\times\left(\frac{\mathbf{b}}{\hat{B}}\right)\cdot\hat{\nabla}\hat{T}_e,\end{aligned}$$

(electron continuity) (A.1)

$$\begin{aligned}\frac{\partial\hat{\chi}_i}{\partial\hat{t}} = &-\frac{1}{\hat{B}}\mathbf{b}\cdot\hat{\nabla}\hat{\phi}\times\hat{\nabla}\hat{V}_{i\parallel} - \hat{V}_{i\parallel}\hat{\nabla}_\parallel\hat{V}_{i\parallel} - \hat{\nabla}_\parallel\hat{\phi} - \frac{\hat{\nu}_\parallel}{\mu}\left(\hat{V}_{i\parallel} - \hat{V}_{e\parallel}\right)\\ &-\frac{\hat{V}_{i\parallel}\hat{S}}{\hat{n}} + 0.71\hat{\nabla}_\parallel\hat{T}_e - \hat{\nabla}_\parallel\hat{p}_i - \frac{2\hat{B}^{3/2}}{3\hat{n}}\hat{\nabla}_\parallel\left(\frac{\hat{\pi}_{ci}}{\hat{B}^{3/2}}\right),\end{aligned}$$

(parallel ion momentum) (A.2)

$$\begin{aligned}\frac{\partial\hat{\chi}_e}{\partial\hat{t}} = &-\frac{1}{\hat{B}}\mathbf{b}\cdot\hat{\nabla}\hat{\phi}\times\hat{\nabla}\hat{V}_{e\parallel} - \hat{V}_{e\parallel}\hat{\nabla}_\parallel\hat{V}_{e\parallel} + \mu\hat{\nabla}_\parallel\hat{\phi}\\ &+\hat{\nu}_\parallel\left(\hat{V}_{i\parallel} - \hat{V}_{e\parallel}\right) - \mu\hat{T}\hat{\nabla}_\parallel\log\hat{n} - 1.71\mu\hat{\nabla}_\parallel\hat{T}_e - \frac{\hat{V}_{e\parallel}\hat{S}}{\hat{n}},\end{aligned}$$

(Ohm's law) (A.3)

$$\begin{aligned}\frac{\partial\hat{\Omega}}{\partial\hat{t}} = &-\hat{\nabla}\cdot\left(\frac{1}{\hat{B}}\mathbf{b}\cdot\hat{\nabla}\phi\times\hat{\nabla}\hat{\boldsymbol{\omega}}\right)\\ &-\hat{B}\nabla_\parallel\left(\frac{1}{\hat{B}}\hat{V}_{i\parallel}\hat{\Omega}\right) - \hat{\nabla}_\perp\left(\hat{B}\hat{\nabla}_\parallel\left(\frac{\hat{V}_{i\parallel}}{\hat{B}}\right)\right)\cdot\hat{\boldsymbol{\omega}} - \hat{\nabla}_\perp\hat{V}_{i\parallel}\cdot\hat{\nabla}_\parallel\hat{\boldsymbol{\omega}}\\ &+\hat{B}\hat{\nabla}_\parallel\left(\frac{\hat{V}_{i\parallel} - \hat{V}_{e\parallel}}{\hat{B}}\right) + \left(\hat{V}_{i\parallel} - \hat{V}_{e\parallel}\right)\hat{\nabla}_\parallel\log\hat{n}\\ &+\hat{\mu}_\Omega\hat{\nabla}_\perp^2\hat{\Omega} + \hat{\nabla}_\perp\hat{\mu}_\Omega\cdot\hat{\nabla}_\perp\hat{\Omega} + \frac{1}{6}\hat{\nabla}\times\left(\frac{\mathbf{b}}{\hat{B}}\right)\cdot\hat{\nabla}\hat{\pi}_{ci}\end{aligned}$$

$$+\hat{T}_e\hat{\nabla}\times\left(\frac{\mathbf{b}}{\hat{B}}\right)\cdot\hat{\nabla}\hat{n}+\hat{n}\hat{\nabla}\times\left(\frac{\mathbf{b}}{\hat{B}}\right)\cdot\hat{\nabla}\hat{T}_e$$
$$+\hat{T}_i\hat{\nabla}\times\left(\frac{\mathbf{b}}{\hat{B}}\right)\cdot\hat{\nabla}\hat{n}+\hat{n}\hat{\nabla}\times\left(\frac{\mathbf{b}}{\hat{B}}\right)\cdot\hat{\nabla}\hat{T}_i,$$

(vorticity) (A.4)

$$\begin{aligned}\frac{\partial\log\hat{T}_e}{\partial\hat{t}}=&-\frac{1}{\hat{B}}\mathbf{b}\cdot\hat{\nabla}\hat{\phi}\times\hat{\nabla}\log\hat{T}_e-\hat{V}_{e\parallel}\hat{\nabla}_\parallel\log\hat{T}_e-\frac{2}{3\hat{p}_e}\hat{B}\hat{\nabla}_\parallel\left(\frac{\hat{q}_{e\parallel}}{\hat{B}}\right)\\&-\frac{2}{3}0.71\left(\hat{V}_{i\parallel}-\hat{V}_{e\parallel}\right)\hat{\nabla}_\parallel\log\hat{T}_e-\frac{2}{3}\hat{B}\hat{\nabla}\left(\frac{\hat{V}_{e\parallel}}{\hat{B}}\right)\\&+\frac{2}{3\mu}\frac{\hat{\nu}_\parallel}{\hat{T}_e}\left(\hat{V}_{i\parallel}-\hat{V}_{e\parallel}\right)^2+\frac{2\hat{S}_E}{3\hat{n}\hat{T}_e}+\frac{\hat{V}_{e\parallel}^2\hat{S}}{3\mu\hat{p}_e}-\frac{\hat{S}}{\hat{n}}\\&+\frac{2}{3\hat{n}}\hat{\kappa}_{e\perp}\left(\hat{\nabla}_\perp^2\log\hat{T}_e+\hat{\nabla}_\perp\log\hat{T}_e\cdot\hat{\nabla}_\perp\log\hat{T}_e\right)\\&+\frac{2}{3\hat{n}}\hat{\nabla}_\perp\hat{\kappa}_{e\perp}\cdot\hat{\nabla}_\perp\log\hat{T}_e-\frac{2}{3}\hat{\nabla}\times\left(\frac{\mathbf{b}}{\hat{B}}\right)\cdot\hat{\nabla}\hat{\phi}\\&+\frac{2\hat{T}}{3\hat{n}}\hat{\nabla}\times\left(\frac{\mathbf{b}}{\hat{B}}\right)\cdot\hat{\nabla}\hat{n}+\frac{7}{3}\hat{\nabla}\times\left(\frac{\mathbf{b}}{\hat{B}}\right)\cdot\hat{\nabla}\hat{T}_e-\frac{2}{3\hat{p}_e}\hat{Q}_i,\end{aligned}$$

(electron temperature evolution) (A.5)

$$\begin{aligned}\frac{\partial\log\hat{T}_i}{\partial\hat{t}}=&\frac{1}{\hat{B}}\mathbf{b}\cdot\hat{\nabla}\hat{\phi}\times\hat{\nabla}\log\hat{T}_i-\hat{V}_{i\parallel}\hat{\nabla}_\parallel\log\hat{T}_i+\frac{2}{3\hat{p}_i}\hat{Q}_i-\frac{2\hat{B}}{3\hat{p}_i}\hat{\nabla}_\parallel\left(\frac{\hat{q}_{i\parallel}}{\hat{B}}\right)\\&+\frac{2}{3}\hat{\nabla}\times\left(\frac{\mathbf{b}}{\hat{B}}\right)\cdot\hat{\nabla}\hat{T}_e+\frac{2}{3}\frac{\hat{T}_e}{\hat{n}}\hat{\nabla}\times\left(\frac{\mathbf{b}}{\hat{B}}\right)\cdot\hat{\nabla}\hat{n}\\&-\frac{2}{3}\hat{\nabla}\times\left(\frac{\mathbf{b}}{\hat{B}}\right)\cdot\hat{\nabla}\hat{\phi}-\frac{5}{3}\hat{\nabla}\times\left(\frac{\mathbf{b}}{\hat{B}}\right)\cdot\hat{\nabla}\hat{T}_i\\&-\frac{2\hat{B}}{3}\hat{\nabla}_\parallel\left(\frac{\hat{V}_{e\parallel}}{\hat{B}}\right)+\frac{2}{3\hat{n}}\left(\hat{V}_{i\parallel}-\hat{V}_{e\parallel}\right)\hat{\nabla}_\parallel\hat{n}\\&-\frac{4}{9\hat{p}_i}\hat{\pi}_{ci}\frac{1}{\sqrt{\hat{B}}}\hat{\nabla}_\parallel\left(\sqrt{\hat{B}}\hat{V}_{i\parallel}\right)+\frac{2\hat{S}_{Ei}}{3\hat{p}_i}+\frac{\hat{V}_{i\parallel}^2\hat{S}}{3\hat{p}_i}-\frac{\hat{S}}{\hat{n}}\\&+\frac{2}{3\hat{n}}\hat{\kappa}_{i\perp}\left(\hat{\nabla}_\perp^2\log\hat{T}_i+\hat{\nabla}_\perp\log\hat{T}_i\cdot\hat{\nabla}_\perp\log\hat{T}_i\right)\\&+\frac{2}{3\hat{n}}\hat{\nabla}_\perp\hat{\kappa}_{i\perp}\cdot\hat{\nabla}_\perp\log\hat{T}_i,\end{aligned}$$

(ion temperature evolution) (A.6)

where $\mu = m_i/m_e$. We have used the normalised variables $\hat{\Omega} = \hat{\nabla}\cdot\hat{\boldsymbol{\omega}}$, with $\hat{\boldsymbol{\omega}} = \left(\hat{n}\hat{\nabla}_\perp\hat{\phi}+\hat{\nabla}_\perp\hat{p}_i\right)/\hat{B}^2$, $\hat{p}_i = \hat{n}\hat{T}_i$, $\hat{\chi}_i = \hat{V}_{i\parallel}+\mu_0 n_0 T_0\hat{\psi}/B_0^2$ and $\hat{\chi}_e = \hat{V}_{i\parallel}-\mu\mu_0 n_0 T_0\hat{\psi}/B_0^2$; fluxes $\hat{q}_{e\parallel} = q_{e\parallel}/n_0 c_{s0} T_0$, and $\hat{q}_{i\parallel} = q_{i\parallel}/n_0 c_{s0} T_0$; and energy exchange $\hat{Q}_i = Q_i/n_0 T_0\Omega_{i0}$. The normalised parallel $\hat{\nu}_\parallel = 0.51/\tau_e\Omega_{i0}$, $\hat{\pi}_{ci} = \pi_{ci}/n_0 T_0$, and perpendicular $\hat{D}_\perp = D_\perp/\rho_{s0}^2\Omega_{i0}$, $\hat{\mu}_\Omega = \mu_\Omega/\rho_{s0}^2\Omega_{i0}$, $\hat{\kappa}_{e\perp} = \kappa_{e\perp}/n_0\rho_{s0}^2\Omega_{i0}$, $\hat{\kappa}_{i\perp} = \kappa_{i\perp}/n_0\rho_{s0}^2\Omega_{i0}$ dissipation

parameters are used, and finally the normalised source terms applied are $\hat{S} = S/n_0\Omega_{i0}$, $\hat{S}_E = S_E/n_0T_0\Omega_{i0}$ and $\hat{S}_{Ei} = S_{Ei}/n_0T_0\Omega_{i0}$.

References

[1] A. Loarte, B. Lipschultz, A. S. Kukushkin, G. F. Matthews, P. C. Stangeby, N. Asakura, G. F. Counsell, G. Federici, A. Kallenbach, K. Krieger, A. Mahdavi, V. Philipps, D. Reiter, J. Roth, J. Strachan, D. Whyte, R. Doerner, T. Eich, W. Fundamenski, A. Herrmann, M. Fenstermacher, P. Ghendrih, M. Groth, A. Kirschner, S. Konoshima, B. LaBombard, P. Lang, A. W. Leonard, P. Monier-Garbet, R. Neu, H. Pacher, B. Pegourie, R. A. Pitts, S. Takamura, J. Terry, E. Tsitrone and the ITPA Scrape-off Layer and Divertor Physics Topical Group, *Nucl. Fusion* **47** S203 (2007).

[2] S. I Krasheninnikov, *Phys. Lett. A* **283** 368 (2001).

[3] J. A. Boedo, D. Rudakov, R. Moyer, S. Krasheninnikov, D. Whyte, G. McKee, G. Tynan, M. Schaffer, P. Stangeby, P. West, S. Allen, T. Evans, R. Fonck, E. Hollmann, A. Leonard, A. Mahdavi, G. Porter, M. Tillack, and G. Antar , *Phys. Plasmas* **8** 4826-4833 (2001).

[4] D. L. Rudakov, J. A. Boedo, R. A. Moyer, S. Krasheninnikov, A. W. Leonard, M. A. Mahdavi, G. R. McKee, G. D. Porter, P. C. Stangeby, J. G. Watkins, W. P. West, D. G. Whyte and G. Antar, *Plasma Phys. Control. Fusion* **44** 717 (2002).

[5] R. D. Hazeltine and J. D. Meiss, *Phys. Reports* **121** 1 (1985).

[6] W. M. Tang, C. S. Liu, M. N. Rosenbluth, P. J. Catto and J. D. Callen, *Nucl. Fusion* **16** 191 (1976).

[7] P. Helander and D. J. Sigmar, *Collisional Transport in Magnetized Plasmas*, (*Cambridge University Press, Cambridge, 2002*).

[8] D. A. D'Ippolito, J. R Myra and S. J. Zweben, *Phys. Plasmas* **8** 060501 (2011).

[9] S. Y. Allan, S. Elmore, G Fishpool, *et al.*, *Plasma Phys. Control. Fusion* **58** 045014 (2016).

[10] M. Kocan, J. P. Gunn, S. Carpentier-Chouchana, *et al.*, *J. Nuc. Mat.* **415** S1133 (2011).

[11] J. Adamek, D. Cipciar, A. Devitre, J. Horacek, J. Cavalier, M. Komm, J. Krbec, M. Tichy, D. Trunec, P. Böhm, R. Panek and the COMPASS team, *Nucl. Fusion* **61** 036023 (2021).

[12] S. I. Braginskii, *Rev. Plasma Phys.*, ed. M. A. Leontovich, (*Consultants Bureau, New York, 1965*), *Vol. 1* p205.

[13] O. E. Garcia, N. H. Bian, V Naulin, A. H. Nielsen and J. Juul Rasmussen, *Phys. Plasmas* **12** 090701 (2005).

[14] J. R. Myra, D. A. D'Ippolito, S. I. Krasheninnikov and G. Q. Yu, *Phys. Plasmas* **11** 4267 (2004).

[15] L. Easy, F. Militello, J. Omotani, N. R. Walkden and B. Dudson, *Phys. Plasmas* **23** 012512 (2016).

[16] D. D. Ryutov, *Phys. Plasmas* **13** 122307 (2006).

[17] N. R. Walkden, B. D. Dudson, and G. Fishpool, *Plasma Phys. Control. Fusion* **55** 105005 (2013).

[18] O. E. Garcia, V Naulin, A. H. Nielsen and J. Juul Rasmussen, *Phys. Plasmas* **12** 062309 (2005).

[19] D. Jovanovic, P. K. Shukla, and F. Pegoraro, *Phys. of Plasmas* **15** 112305 (2008).

[20] F. Nespoli, P. Tamain, N. Fedorczak, G. Ciraolo, D. Galassi, R. Tatali, E. Serre, Y. Marandet, H. Bufferand and Ph. Ghendrih, *Nucl. Fusion* **59** 096006 (2019).

[21] N. Bisai, R. Singh, and P. K. Kaw, *Phys. Plasmas* **19** 052509 (2012).

[22] J. Madsen, O. E. Garcia, J. S. Larsen, *et al.*, *Phys. Plasmas* **18** 112504 (2011).

[23] A. H. Nielsen, J. J. Rasmussen, J. Madsen, *et al.*, *Plasma Phys. Control. Fusion* **59** 025012 (2017).

[24] P. Manz, D. Carralero, G. Birkenmeier, *et al.*, *Phys. Plasmas* **20** 102307 (2013).

[25] W. Lee, M. V. Umansky, J. R. Angus, and S. I. Krasheninnikov, *Phys. Plasmas* **22** 012505 (2015).

[26] S. Krasheninnikov, D. Ryutov, and G. Yu, *J. Plasma Fus. Res.* **6** 139 (2004).

[27] N. Katz, J. Egedal, W. Fox, A. Le, and M. Porkolab, *Phys. Rev. Lett.* **101** 015003 (2008).

[28] C. Theiler, I. Furno, *et al.*, *Phys. Rev. Lett.* **103** 065001 (2009).

[29] B. D. Dudson, M. V. Umansky, X. Q. Xu, P. B. Snyder, and H. R. Wilson, *Comput. Phys. Commun.* **180** 1467 (2009).
[30] B. D. Dudson, J. Madsen, J. Omotani, P. Hill, L. Easy, and M. Løiten, *Phys. Plasmas* **23** 062303 (2016).
[31] N. R. Walkden, L. Easy, F. Militello and J. T. Omotani, *Plasma Phys. Control. Fusion* **58** 115010 (2016).
[32] D. Hoare, F. Militello, J. T. Omotani, *et al.*, *Plasma Phys. Control. Fusion* **61** 105013 (2019).
[33] B. D. Dudson, S. L. Newton, J. T. Omotani and J. Birch, *Plasma Phys. Control. Fusion* **63** 125008 (2021).
[34] F. Militello, B. D. Dudson, L. Easy, A. Kirk and P. Naylor, *Plasma Phys. Control. Fusion* **59** 125013 (2017).
[35] G. Q. Yu, S. I. Krasheninnikov and P. N. Guzdar, *Phys. Plasmas* **13** 042508 (2006).
[36] J. R. Angus and S. I. Krasheninnikov, *Phys. Plasmas* **21** 112504 (2014).
[37] F.D. Halpern, P. Ricci, S. Jolliet, J. Loizu, J. Morales, A. Mosetto, F. Musil, F. Riva, T.M. Tran and C. Wersal, *J. Comp. Phys.* **315** 388 (2016).
[38] A. Mosetto, F. D. Halpern, S. Jolliet, J. Loizu and P. Ricci, *Phys. Plasmas* **22** 012308 (2015).
[39] P. Ricci, F. D. Halpern, S. Jolliet, J. Loizu, A. Mosetto, A. Fasoli, I. Furno and C. Theiler, *Plasma Phys. Control. Fusion* **54** 124047 (2012).
[40] A. B. Mikhailovskii and V. S. Tsypin, *Beitr. Plasmaphys.* **24** 335 (1984).
[41] P. J. Catto and A. N. Simakov, *Phys. Plasmas* **11** 90 (2004).
[42] A. N. Simakov and P. J. Catto, *Phys. Plasmas* **10** 4744 (2003).
[43] J. T. Omotani, D. Dickinson, B. D. Dudson, L. Easy, D. Hoare, P. A. Hill, T. Nicholas, J. Parker, and F. Riva, N. Walkden, Q. Xia, and F. Militello, "STORM: Scrape-off layer turbulence in tokamak fusion reactors", *in preparation.*
[44] A. C. Hindmarsh, P. N. Brown, K. E. Grant, S. L. Lee, R. Serban, D. E. Shumaker, and C. S. Woodward, *ACM Trans. Math. Softw.*, **31(3)** 363 (2005).
[45] L. Easy, "3D Simulations of Scrape-Off Layer Filaments", PhD thesis, University of York (2016).
[46] G. Q. Yu and S. I. Krasheninnikov, *Phys. Plasmas* **10** 4413 (2003).
[47] W. Fundamenski, O.E. Garcia, V. Naulin, R.A. Pitts, A.H. Nielsen, J. Juul Rasmussen, J. Horacek, J.P. Graves and JET EFDA contributors, *Nucl. Fusion* **47**, 417 (2007).
[48] L. Easy, F. Militello, J. Omotani, B. Dudson, E. Havlíčková, P. Tamain, V. Naulin, and A. H. Nielsen, *Phys. Plasmas* **21**, 122515 (2014).
[49] F. Militello, N.R. Walkden, T. Farley, W.A. Gracias, J. Olsen, F. Riva, L. Easy, N. Fedorczak, I. Lupelli, J. Madsen, A.H. Nielsen., P. Ricci, P. Tamain and J. Young, *Plasma Phys. Control. Fusion* **58**, 105002 (2016).
[50] T. Farley, N.R. Walkden, F. Militello, M. Sanna, J. Young, S.S. Silburn, J. Harrison, L. Kogan, S.S. Henderson, I. Lupelli, A. Kirk, and J.W. Bradley, *Rev. Sci. Instrum.* **90**, 093502 (2019).
[51] A. Kirk, A.J. Thornton, J.R. Harrison, F. Militello, N.R. Walkden and the MAST Team and the EUROfusion MST1 Team, *Plasma Phys. Control. Fusion* **58**, 085008 (2016).
[52] P. C. Stangeby, *The Plasma Boundary of Magnetic Fusion Devices*, (*CRC Press, Boca Raton, 2000*).
[53] A. Ross and A. Stegmeir and D. Coster, *Contrib. Plasma Phys.* **58**, 478 (2018).
[54] W. W. Lee, *J. Comp. Phys.* **72**, 243 (1987).
[55] B. F. McMillan, *Phys. Plasmas* **27**, 052106 (2020).
[56] J. Angus and S.I. Krasheninnikov and M. V. Umansky, *Phys. Plasmas* **19**, 082312, (2012).
[57] N. R. Walkden and B. D. Dudson and L. Easy and G. Fishpool and J. T. Omotani, *Nucl. Fusion* **55**, 113022 (2015).